Journal of Power Sources 196 (2011) 6456–6464

Contents lists available at ScienceDirect

Journal of Power Sources

journal homepage: www.elsevier.com/locate/jpowsour

Correlation between micro-structural properties and ionic conductivity of $Li_{1.5}Al_{0.5}Ge_{1.5}(PO_4)_3$ ceramics

Chinnasamy R. Mariappan [a,*], Chihiro Yada [b], Fabio Rosciano [c], Bernhard Roling [a]

[a] Department of Chemistry, University of Marburg, Hans-Meerwein-Strasse, D – 35032 Marburg, Germany
[b] Battery Research Division, Toyota Motor Corp., Higashifuji Technical Center 1200, Mishuku, Susono, Shizuoka 410-1193 Japan
[c] Advanced Technology 1 Division, Toyota Motor Europe, Hoge Wei 33, B - 1930 Zaventem, Belgium

ARTICLE INFO

Article history:
Received 29 December 2010
Received in revised form 20 February 2011
Accepted 27 March 2011
Available online 6 April 2011

Keywords:
LAGP ceramics
Flash creation method
Ionic conductivity
Brick layer model
Finite element approach

ABSTRACT

We report on the structure and lithium ion transport properties of $Li_{1.5}Al_{0.5}Ge_{1.5}(PO_4)_3$ (LAGP). This material is commercially available and is prepared as amorphous powders via a flame spray technique called Flash Creation Method (FCM). We crystallize and sinter the amorphous powders at different temperatures in order to alter grain size and grain boundary properties. The structure is then characterized by means of powder X-ray diffraction, atomic force microscopy, scanning electron microscopy and transmission electron microscopy with energy dispersive X-ray spectroscopy. AC impedance spectroscopy is used to study lithium ion transport. A maximum total conductivity of 2×10^{-4} S cm^{-1} at room temperature is found for a sample sintered at 750 °C for 2 h. In order to distinguish between grain and grain boundary contributions to the impedance spectra, equivalent circuit fits are carried out. The results are analysed in the framework of the classical brick layer model and of a finite-element approach taking into account non-ideal grain contacts. Our experimental results for the grain and grain boundary resistances are in good agreement with the predications of the finite-element approach.

1. Introduction

In recent years, lithium-ion conducting solids have been investigated for potential applications as electrolytes in solid-state lithium batteries and other electrochemical devices [1–4]. In particular, high lithium ion conductivity and high electrochemical stability at room temperature are desired properties. Most of the discovered lithium ion conductors, such as Li_3N, Li-β alumina, LISICON ($Li_{2+2x}Zn_{1-x}GeO_4$), LIPON (xLi_2O–yP_2O_5–zPON; PON = phosphorous oxynitride), lithium sulphide glasses (Li_2S–P_2O_5–LiI and Li_2S–SiS_2–Li_3PO_4), Li-analogues of NASICON ($Li_{1+x}M_{2-x}M'_xP_3O_{12}$, M = Ti, Zr, Hf, Ge, Sn; M′ = Al, Ga, In) and perovskite-type lithium lanthanum titanate ($Li_{3x}La_{(2/3)-x\,(1/3)-2x}TiO_3$) have either high ionic conductivity or high electrochemical stability, but not both [4–10]. However, the Li-analogues of NASICON-type compounds $LiM_2(PO_4)_3$ (M is one or more tri-, tetra- and pentavalent ions) have received much attention as prospective solid electrolytes due to their high ionic conductivity and high stability against moisture [3,9,11–13].

The structure of crystalline NASICON (acronym of Na^+ Super Ionic Conductor) compounds is optimal for fast alkali ion conduction [14]. In contrast, glassy NASICON compounds exhibit a much lower ionic conductivity [15,16]. The crystalline NASICON skeleton consists of MO_6 octahedra and PO_4 tetrahedra units. These units are corner-sharing, resulting in a three-dimensional network structure. Two different lithium-ion sites, I and II, exist in the structure. For $LiM_2(PO_4)_3$ compounds containing exclusively tetravalent M^{4+} ions (M = Ti, Zr, Hf, Ge, Sn), the I sites are fully occupied, while the II sites are completely vacant. [3,14] When the tetravalent ions are partially substituted by trivalent ion $(M')^{3+}$ (M′ = Al, Ga, In), the additional Li^+ ions in the $Li_{1+x}M_{2-x}M'_xP_3O_{12}$ compounds occupy the II sites [3,9]. The partial substitution can lead to an enhancement of the lithium ion conductivity by more than two orders of magnitude.

The highest ionic conductivities in polycrystalline Li-analogues of NASICONs have been found for compounds containing Ti^{4+} ions (conductivities up to 10^{-3} S cm^{-1} at room temperature) [3]. However, a major drawback of these compounds is the easy reduction of the Ti^{4+} by typical anode materials in batteries (e.g. lithium metal, lithiated graphite). Therefore, there have been considerable efforts to synthesize and characterize Ti-free Li-analogues of NASICONs in the form of sintered polycrystals [11,13,17]. The compound $Li_{1+x}Al_xGe_{2-x}(PO_4)_3$ (LAGP) with $x = 0.5$ is one the most promising candidates [9,17].

The total conductivity of polycrystalline materials does not only depend on lithium ion transport in the crystalline grains, but also through the grain boundaries [17]. If the serial grain boundary

* Corresponding author. Tel.: +49 6421 28 22312; fax: +49 6421 28 22309.
E-mail addresses: mariappa@staff.uni-marburg.de, crmari2005@yahoo.com (C.R. Mariappan).

0378-7753/$ – see front matter © 2011 Elsevier B.V. All rights reserved.
doi:10.1016/j.jpowsour.2011.03.065

resistance is much higher than the grain resistance, it determines the overall resistance of the material in an electrochemical cell. Therefore, controlling the structure and the ion transport properties of the grain boundaries is a key factor for obtaining optimised NASICON-type room temperature solid electrolytes.

Different models describing the influence of grain boundaries on the electrical properties of solid electrolytes are available in the literature. These are in particular: (i) the classical brick layer model (BLM), (ii) a generalized brick layer model taking into account parallel grain boundary conduction and (iii) the nano-grain composite model [18–20]. Fleig and co-workers have extensively investigated the limitations of the classical BLM description using finite element simulations of microstructures with varying grain shape, grain size distribution, imperfect contacts between grains (porosity or secondary phases) and inhomogeneous grain boundary conductivity [21,22]. They demonstrated that imperfect contacts between grains can lead to significant deviations of the impedance spectra from predictions of the classical BLM. On the other hand, deviations caused by grain size distributions are relatively weak.

An alternative to the solid-state synthesis of polycrystalline materials is the preparation of glass ceramics by controlled crystallisation of parent glasses [23]. This method allows for an easier preparation of the desired shape, grain size and grain boundary properties. Most studies have been reported so far on $Li_{1.5}Al_{0.5}Ge_{1.5}(PO_4)_3$ glass-ceramics. Depending on the sintering conditions used for crystallisation process, total room-temperature lithium ion conductivities in the range of 10^{-3}–10^{-5} S cm^{-1} have been found [23–29]. However, the ion transport properties of the grain boundaries are scarcely understood up to now.

If the parent LAGP glass is prepared by melt quenching, the high melting temperatures above 1350 °C lead to lithium losses [30]. Therefore, there is a strong need for lower temperature preparation methods, such as solution and combustion methods [31,32]. In this study, LAGP ceramics were fabricated from amorphous powders, which were prepared by the flash creation method. The average grain size of the ceramics could be controlled by the sintering temperature and time. The structural properties were characterized by means of temperature-dependent powder X-ray diffraction, atomic force microscopy, scanning electron microscopy and transmission electron microscopy with energy dispersive X-ray analysis. The lithium ion transport was studied by means of AC impedance spectroscopy. The grain and grain boundary contributions to the impedance spectra were analysed and interpreted in the framework of the classical BLM and of a finite-element approach taking into account non-ideal grain contacts. Evidence for non-ideal grain contacts were found in the TEM studies.

2. Experimental

Amorphous LAGP powder was obtained from Hosokawa Micron Corporation, Japan. The Hosokawa Micron Corporation synthesized the amorphous LAGP powder by the so-called "flash creation method" (FCM), in which amorphous LAGP powder was obtained by drying the precursor solution by fire injection. The precursor solution contained the following components: (1) Lithium naphthenate solution (Li concentration: 1.2 wt.%), (2) ethylacetoacetate-aluminum-di-n-butyrate solution (Al concentration: 5.8 wt.%), (3) germanium-dissolved mineral spirit solution (Ge concentration: 9.8 wt.%) and (4) di-ethyl-phosphonoacetic acid (P concentration: 13.4 wt.%). Mineral spirit was used as the diluting solvent. The total metal (Li + Al + Ge + P) concentration in the precursor solution was 3.1 wt.%. During the synthesis, oxygen gas with 30 L min^{-1} was flowed to the nozzle. The atmosphere inside the chamber was a mixture of air and oxygen with the pressure of 10^4 Pa. The average size of the amorphous FCM-LAGP powder is 100 nm. More details of the flash creation method can be found elsewhere [32,33].

Thermogravimetric analysis (TGA) and differential scanning calorimetry (DSC) were performed on the FCM-LAGP powder using a NETZSCH instrument model STA 409C/CD. The temperature was varied from room temperature to 1000 °C with a heating rate of 5 °C min^{-1} and 10 °C min^{-1}, respectively, in N_2 atmosphere.

Partially and completely crystallised $Li_{1.5}Al_{0.5}Ge_{1.5}(PO_4)_3$ (LAGP) powders were obtained by sintering the amorphous FCM-LAGP powder for 2 h at different temperatures in the range of 520 °C–950 °C.

Powder X-ray diffraction (XRD) patterns of glassy and nanocrystalline LAGP powders were recorded at a room temperature using a Philips X'Pert PRO diffractometer, equipped with a X'celerator detector using monochromated Cu-Kα radiation. The XRD patterns of the sintered powders were recorded in the range $2\theta = 10 - 90^\circ$ with an interpolation step of 0.0167°. The data were used for refining the crystal structure by the Rietveld method with the Fullprof program [34]. The average crystallite size of each sintered sample was estimated using the Williamson–Hall [35] analysis of powder XRD data.

The glassy LAGP powders were coaxially pressed into pellets (10 mm of diameter and ~2.0 mm of thickness) using 1 GPa pressure for at least 3 h. Controlled crystallisation was achieved by sintering for 2 h at different temperatures (520 °C–950 °C) under air. After sintering, these pellets were characterized by density measurements, atomic force microscopy, scanning electron microscopy, transmission electron microscopy with energy dispersive X-ray spectroscopy analyses and ac impedance spectroscopy.

The relative density of the samples was calculated from the ratio of experimental density and to theoretical density. The theoretical density was derived from the molecular weight of LAGP and the XRD cell parameters, and the experimental density was obtained from measurement of weight and volume of the sintered each pellet.

Atomic force microscopy was performed on the cross-section of broken samples using the Solver scanning probe microscope P47 (NT-MDT) operating in contact mode. The scanning electron microscopy (SEM) investigations were also conducted on the cross-section of the broken samples using a JEOL Field Emission SEM model JSM-7500F. Samples were gold sputtered to eliminate any charging effect. Furthermore transmission electron microscopy with energy dispersive X-ray spectroscopy (TEM/EDX) analysis was carried out on the sintered pellets in order to obtain the chemical/structural information at grain and grain boundary regions.

For AC impedance measurements, gold or platinum were coated on both faces of the sintered each pellet using a BAL-TEC SCD005 sputter coater. The pellets were then placed in a two-electrode sample cell. AC impedance data were collected using a Novocontrol Alpha-AK impedance analyzer over the frequency range 1 MHz–0.1 Hz, with an applied root mean square AC voltage of 100 mV. The measurements were carried out at temperatures between −100 °C to +150 °C, the temperature being controlled by the Novocontrol Quatro Cryosystem. The maximum temperature variation tolerated during the impedance measurements was ±0.1K.

3. Results and discussion

3.1. Thermal analysis and XRD

Fig. 1 shows the results of a TGA/DSC study on glassy FCM-LAGP in the temperature range from room temperature to 1000 °C. The TGA curves exhibit only one weight loss step up to about 200 °C. This loss is most likely due to evaporation of moisture or moieties

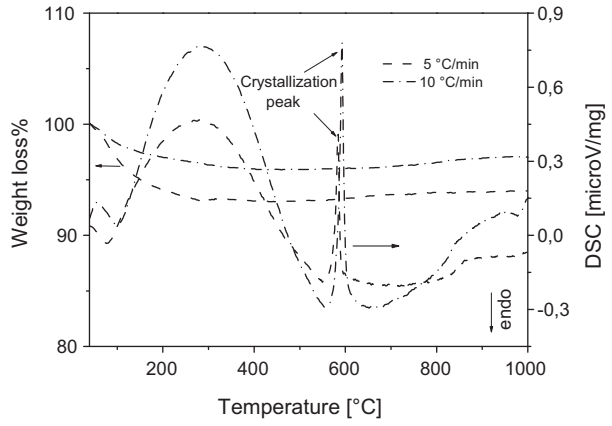

Fig. 1. TGA and DSC curves for amorphous FCM-LAGP powder.

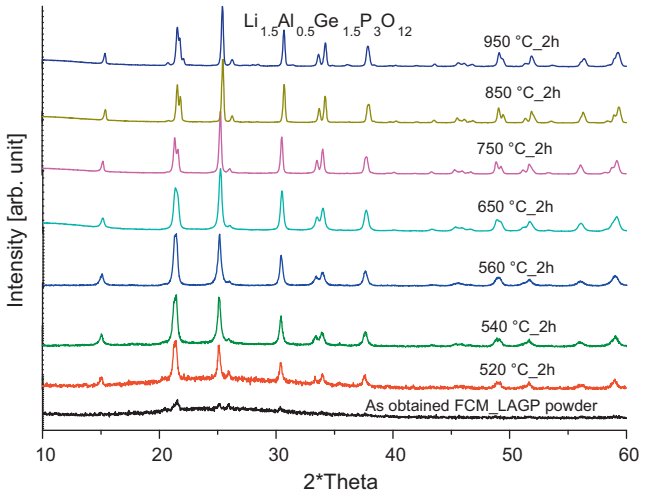

Fig. 2. Powder X-ray diffraction patterns of LAGP samples after sintering at different temperatures for 2 h.

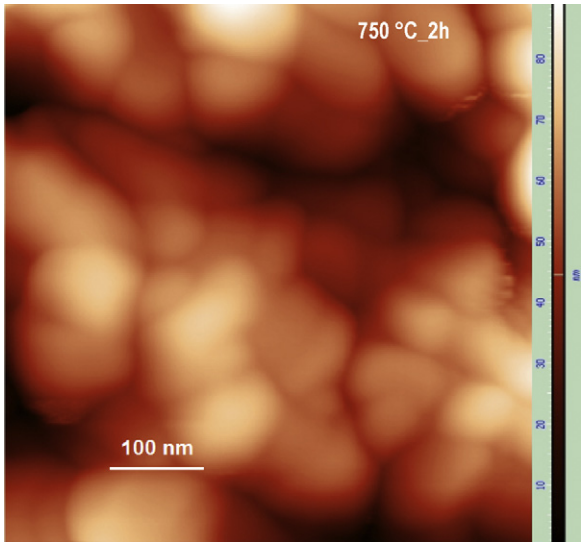

Fig. 3. Atomic force microscope image for a freshly broken LAGP sample which had been sintered at 750 °C for 2h.

from the precursors. An exothermic DSC peak is observed at 584 °C for a heating rate of 5 °C min^{-1} and at 593 °C for a heating rate of 10 °C min^{-1}, respectively. The peak is caused by the crystallization of the amorphous samples. The crystallization temperature of our glassy FCM-LAGP is lower than that of melt-quenched LAGP [23].

Partially and completely crystallised LAGP samples were prepared by sintering the amorphous FCM-LAGP. Variation of the sintering temperature resulted in different mean particle sizes. Fig. 2 shows the room temperature powder XRD patterns of samples sintered at different temperature for 2 h in air. The crystalline NASICON-type phase was observed in the XRD patterns when the sintering temperature was 520 °C or higher. At 520 °C, a characteristic background at low diffraction angles due to residual amorphous phase is detected. At higher sintering temperatures, the background becomes smaller and the diffraction peaks become more intense.

The mean crystallite size of the samples was estimated from the broadening of the Bragg peaks. For this, we used the Williamson–Hall (WM) method which takes into account both the mean grain size D and strain ε effects [35]:

$$\beta^2 = \left(\frac{0.89\,\lambda}{D\,\cos(\theta)}\right)^2 + (4\varepsilon\tan(\theta))^2 + (\beta_0)^2 \quad (1)$$

Here, β is the full width at half maximum (FWHM) of the diffraction peak, θ is the Bragg angle, λ is the wavelength of X-rays (0.154 nm), and β_0 is the instrumental broadening. We have used the most intense XRD peaks between $2\theta = 15°$–$50°$ to estimate β. The obtained mean crystallite size D and strain ε values are shown in Table 1. The mean crystallite size increases from 30 nm at a sintering temperature of 520 °C to 194 nm at a sintering temperature of 950 °C. These values are in good agreement with results obtained by AFM imaging of sintered broken pellets, see Fig. 3.

The refinement of the $Li_{1.5}Al_{0.5}Ge_{1.5}(PO_4)_3$ rhombohedral structure (space group R-3c, #167) was done by a Rietveld analysis of the powder X-ray diffraction patterns [36]. An example for LAGP powder sintered at 950 °C for 2 h is shown in Fig. 4. Initially, the common overall parameters, zero shift, unit-cell parameters, half-width, background, scale factor and pseudo-Voigt coefficient were refined. In the non-stoichiometric phase $Li_{1+x}Al_xGe_{2-x}(PO_4)_3$, the excess lithium is located in the partially occupied II site (Wyckoff site 18e), while Al and Ge share the 12c site. This structure was used throughout the study. Li occupations were not refined, since the electron density of Li is too low. The nominal composition and occupancy of the sites were kept constant for all refinements. Refined

Table 1
Sintering temperatures, mean grain sizes D, strain ε, unit cell parameters and amount of impurity phases for the samples studied in this work.

Sintering temperature	Mean grain size (nm)	Strain	a (±0.007 Å)	c (±0.009 Å)	V (Å^3)	GeO_2 (±0.09%)	$AlPO_4$ (±0.24%)
520 °C	30	0.0032	8.265	20.503	1212.89	–	–
540 °C	35	0.0039	8.260	20.567	1212.89	–	–
560 °C	44	0.0040	8.265	20.571	1215.41	–	–
650 °C	55	0.0036	8.266	20.617	1220.09	–	–
750 °C	76	0.0031	8.266	20.651	1222.22	–	–
850 °C	98	0.0026	8.273	20.651	1224.31	1.40	–
950 °C	194	0.0021	8.279	20.598	1222.97	1.58	4.74

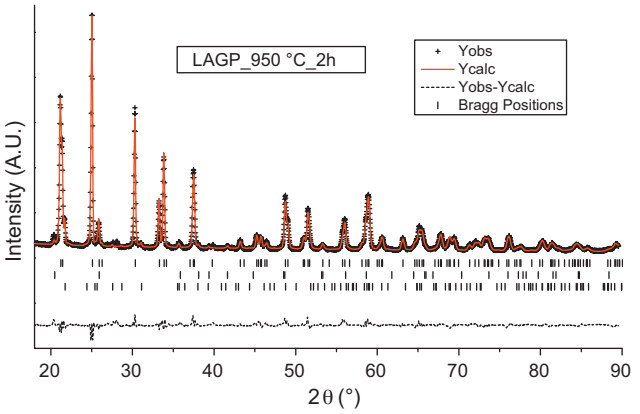

Fig. 4. Observed (+++) calculated (—) and difference powder X-ray diffraction patterns for LAGP sample sintered at 950 °C for 2 h. Vertical bars are related to the calculated Bragg reflections, corresponding from top to bottom to $Li_{1.5}Al_{0.5}Ge_{1.5}P_3O_{12}$, NASICON phase (R-3C, #167), GeO_2 ($P6_222$, #180) and $AlPO_4$ ($C222_1$, #20).

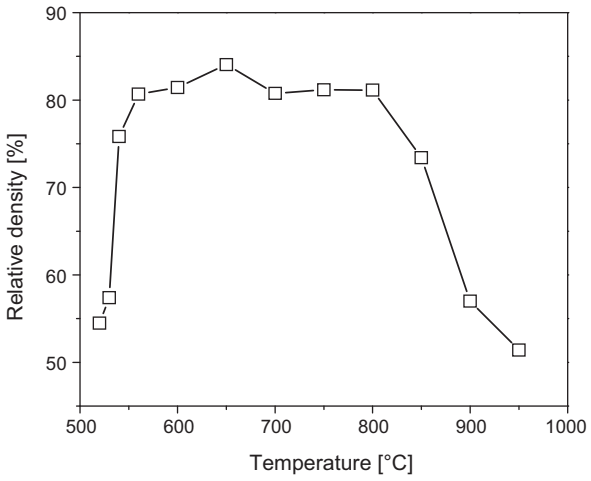

Fig. 5. Relative density of LAGP samples versus sintering temperature.

crystallographic structural parameters and amounts of secondary phases of calcinated LAGP powder are given in Table 1.

From 520 °C to 750 °C, the cell parameter *a* is almost constant, whereas the cell parameter *c* increases. Above 850 °C, the cell parameter *a* increases and *c* decreases. The cell volume increases from 1212.89 Å^3 at 520 °C to 1224.31 Å^3 at 850 °C. When we compared the refined cell parameter of our LAGP samples with microcrystalline material reported by Manso et al., we found that parameter *a* and *c* differ slightly [29], but the cell volumes are in good agreement [17].

The XRD analysis showed that upon heating of the LAGP powder above 800 °C, LAGP decomposes partially resulting in the formation of GeO_2 (space group $P6_222$, #180) [37] and $AlPO_4$ impurity phases (space group $C222_1$, #20) [38], see Table 1.

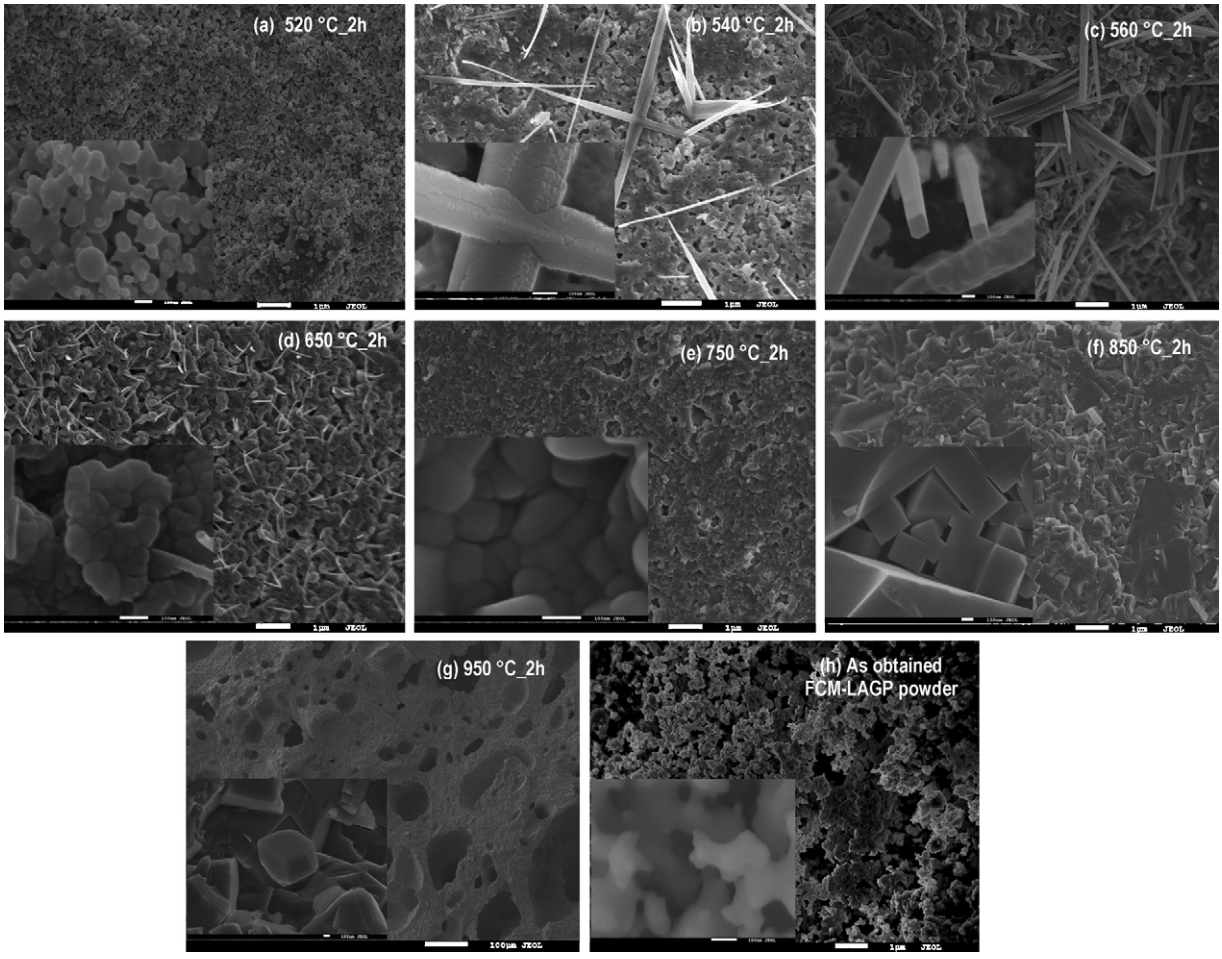

Fig. 6. SEM micrographs of the fracture surface of LAGP pellet sintered for 2 h at (a) 520 °C, (b) 540 °C, (c) 560 °C, (d) 650 °C, (e) 750 °C, (f) 850 °C, (g) 950 °C, and (h) for untreated FCM-LAGP powder.

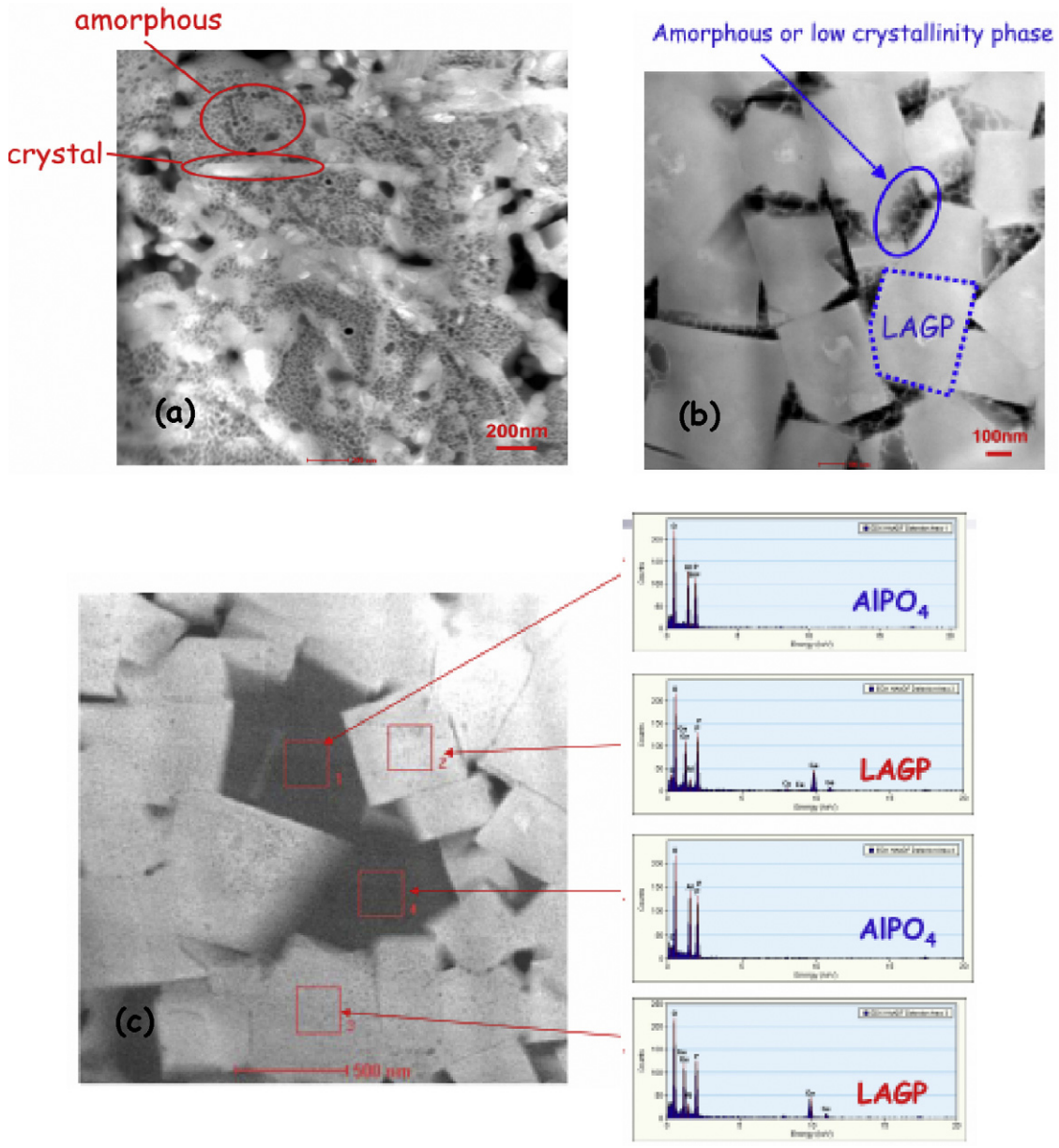

Fig. 7. Dark-field TEM photographs of samples sintered at (a) 540 °C for 2 h, (b) 900 °C for 2 h, and (c) magnified view of sample (b) with EDX information.

3.2. Compactness, SEM and TEM/EDX

In Fig. 5 we show the relative density of the LAGP pellets sintered at different temperatures between 520 °C and 950 °C. The relative density increases from about 50% at 520 °C to more than 80% at 600 °C. From 600 °C to 800 °C, the density is essentially constant, but it decreases strongly above 800 °C. The origin of the decrease above 800 °C is related to a loss of lithium and to the formation of GeO_2 and $AlPO_4$ impurity phases as well as to the formation of pores. The amount of pores increases above 850 °C, as seen in the SEM and TEM/EDX studies (see below).

The relative density of $Li_{1+x}Al_xGe_{2-x}(PO_4)_3$ ceramics prepared by sol–gel methods was reported to be in the range of 70–90% [28] which are in agreement with our samples sintered in the temperature range of 560 °C–800 °C. Samples with higher relative densities (>85%) are not easily achievable with powders prepared via solution and combustion methods. Hot pressing or two-step sintering methods may be helpful [39,40].

SEM photographs of the fractured surface of the LAGP pellets sintered at different temperature for 2 h are shown in Fig. 6(a–g). Fig. 6(h) shows for comparison the SEM picture of the amorphous FCM-LAGP powder. The shape of the particles in the pellet sintered at 520 °C is close to circular and is similar to the amorphous FCM-LAGP powder (Fig. 6(a)). The contact between the particles is poor. This contact is not improved considerably when the sintering temperature is increased to 540 °C (Fig. 6(b)). However, whisker-like rods are observed. In order to further investigate the structure of the whiskers, a TEM/EDX experiment was performed. Fig. 7(a) shows the dark-field TEM picture of a pellet sintered at 540 °C for 2 h. The whisker-like rods exhibit the crystalline nature of LAGP phase. The amorphous phases were easily damaged by the electron beam and converted to foam-like structure. The number of crystalline whisker-like rods is higher at 560 °C and the connectivity of the rods is improved, see Fig. 6(c).

When the sintering temperature is further increased to 650 °C (above the crystallization temperature), the crystalline rods are

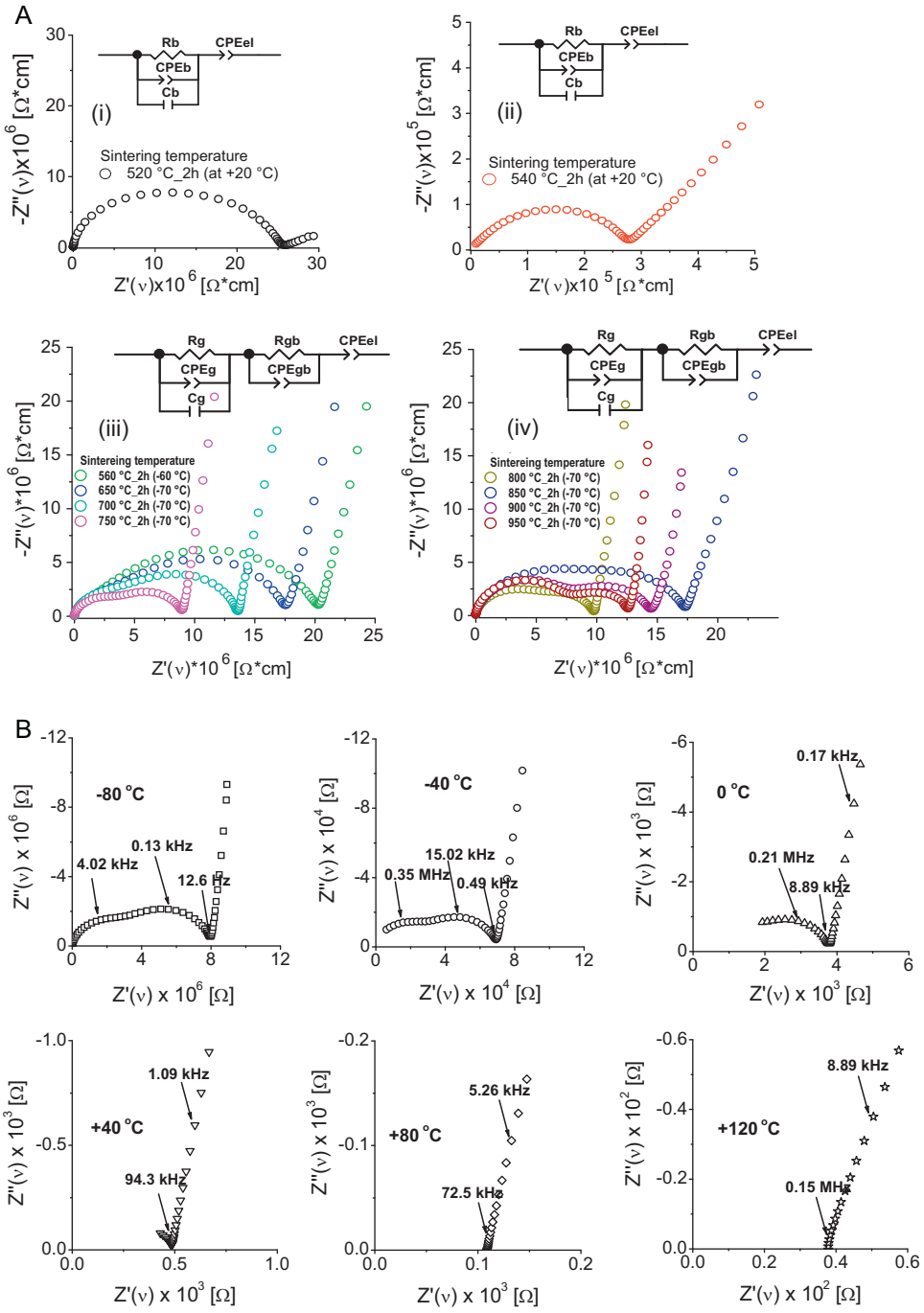

Fig. 8. (A) Complex impedance spectra of LAGP samples sintered for 2 h at (i) 520 °C, (ii) 540 °C and (iii and iv) different temperature between 650 °C and 950 °C. A representative equivalent circuit is shown in the inset of each figure. (B) Nyquist plots of ac impedance at different temperatures for LAGP sample sintered at 750 °C for 2 h.

rehabilitated into fine crystalline grains as shown in the inset of Fig. 6(d). The size of the crystalline grains increases when the sintering temperature is increased to 750 °C, and the contact between the grains is improved, see the inset of Fig. 6(e). This explains the high relative density of the sample. However, pores reducing the relative density are also visible. The grain sizes obtained from the SEM picture is in good agreement with the mean grain size obtained from XRD.

When the sintering temperature is increased to 850 °C, the grains become rectangular in shape, see Fig. 6(f). Sintering at 950 °C leads to a highly porous structure with pore sizes in the range of 1–100 μm, see Fig. 6(g). Thus, sintering above 800 °C leads to significant worsening of the grain contacts.

For sample sintered at 900 °C, the interfaces between the grains were investigated in more detail by TEM/EDX, see Fig. 7(b and c). These studies reveal that there is not only a significant amount of pores at the interfaces, but also amorphous LAGP, LAGP with low crystallinity and $AlPO_4$ impurity phase.

3.3. Impedance spectroscopy

Fig. 8(A) depicts representative complex impedance plots of LAGP pellets sintered at different temperatures between 520 °C and 950 °C for 2 h. The plots were normalized to the geometrical factor the samples t/A, where t and A are the thickness and area of the sample, respectively.

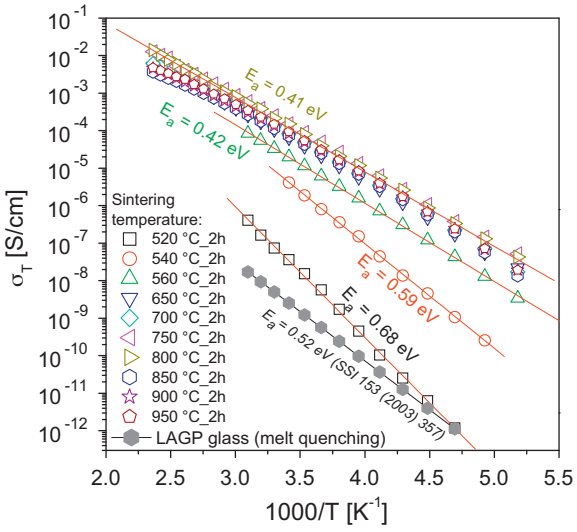

Fig. 9. Arrhenius plot of the total conductivity of LAGP samples sintered at temperatures between 520 °C and 800 °C.

The impedance spectrum of the LAGP pellet sintered at 520 °C shows only a single depressed semicircle at high frequencies and an inclined spike in the low-frequency region, see Fig. 8(A(i)). The semicircle is related to ion conduction in the bulk of the sample, and the inclined spike is related to electrode polarization, i.e. to blocking of the ions at the metal electrodes. The intersection of the semicircle with the real axis gives a high specific resistivity of about $2.6 \times 10^7\ \Omega$ cm, which points to slow lithium ion conduction in the amorphous phase of LAGP. This interpretation is supported by XRD and SEM investigations showing that the amorphous phase is the predominating phase in the sample. In the sample sintered at 540 °C, the bulk resistivity is about $2.8 \times 10^5\ \Omega$ cm, see Fig. 8(A(ii)). This resistivity value is much lower than the resistivity of the amorphous phase, but still considerably higher than expected for lithium ion conduction in crystalline LAGP. Therefore, we suspect that in this sample, the lithium ion transport is still impeded by residual amorphous phase. The samples sintered at temperatures between 560 °C and 950 °C are predominantly crystalline and exhibit a high lithium ion conductivity at room temperature. In order to characterize both grain and grain boundary conductivity, we had to carry out the AC impedance measurements at sub-ambient temperatures, see Fig. 8(A).

Temperature-dependent complex impedance spectra of typical LAGP sample sintered at 750 °C for 2 h are shown in Fig. 8(B). In the Nyquist plots we find two suppressed semicircles, the high-frequency semicircle being related to grain conduction and the low-frequency semicircle to grain boundary conduction. When the measurement temperature is raised above −10 °C, the grain semicircle is outside the frequency window, and the Nyquist plots are governed by grain boundary conduction and electrode polarization. The total resistivity of the samples is obtained from the intercept of the low-frequency semicircle or spike with the real impedance axis.

Results for the temperature dependence of the total conductivity σ_T are shown in Fig. 9. For comparison, we have added total conductivity values of a melt-quenched LAGP glass from the literature [25]. The total conductivity of all samples sintered below 800 °C shows Arrhenius behavior:

$$\sigma_T = A \exp\left(\frac{-E_a}{k_B T}\right) \quad (2)$$

where A is the pre-exponential factor, E_a is the activation energy for conduction, k_B is Boltzmann's constant and T is the absolute temperature. In Table 2 we give values for E_a and for $\log_{10} A$ obtained from Arrhenius fits. The samples sintered above 850 °C show deviations from Arrhenius behavior at measurement temperatures above room temperature. Therefore, the Arrhenius fits were carried out in a temperature range below 20 °C.

Table 2
Pre-exponential factor A and activation energy E_a of total conductivity σ_T for LAGP samples sintered at different temperature.

Sintering temperature	$\text{Log}_{10}(A)$	E_a (eV)
520 °C	4.42 (±0.11)	0.68 (±0.02)
540 °C	4.13 (±0.08)	0.59 (±0.01)
560 °C	2.42 (±0.06)	0.42 (±0.01)
650 °C	2.37 (±0.05)	0.41 (±0.01)
700 °C	2.51 (±0.06)	0.41 (±0.02)
750 °C	2.70 (±0.05)	0.41 (±0.02)
800 °C	2.72 (±0.05)	0.41 (±0.02)
850 °C	2.21 (±0.13)	0.41 (±0.02)
900 °C	2.26 (±0.12)	0.41 (±0.02)
950 °C	2.43 (±0.11)	0.41 (±0.02)

The total conductivity of the samples sintered at 520 °C and 540 °C is lower and the activation energy is higher than for the samples sintered at higher temperatures. As already mentioned above, this is due to slow lithium ion conduction in the amorphous phase of these samples. The total conductivity of the samples sintered at higher temperatures, which are predominantly crystalline, is similar (of the order of 10^{-4} S cm^{-1} at room temperature), and the activation energy is virtually identical (0.41–0.42 eV). A closer inspection reveals that the sample sintered at 750 °C (relative density 83%) exhibits the highest room-temperature conductivity of 2×10^{-4} S cm^{-1}. This value is in good agreement with results reported by Aono et al. [17] on sintered pellet (compactness is >95%) of ball milled powder (particle size < 1 μm) and also with results reported by Cretin and Fabry [28] on sol–gel derived LAGP ceramics.

In contrast, Thokchom et al. reported total room-temperature ionic conductivities of $4–5 \times 10^{-3}$ S cm^{-1} for LAGP glass-ceramics [24,41]. This is more than one order of magnitude higher than the values obtained by other groups. The origin of this discrepancy is related to strong inductance effects in the impedance spectra obtained by Thokchom et al. This is clearly visible in Fig. 4 of Ref. [41]. The intersection of the impedance data with the Z' axis at 501 kHz is caused by the inductance effects, and therefore the Z' value at this frequency (about 270 Ω) cannot be identified with an Ohmic resistance. In a later publication, Thokchom et al. call this apparent resistance a 'circuit resistance'. Using this apparent resistance as a starting point for the fit of a bulk semicircle leads to artificially low resistances and to artificially high conductivities of the samples [24].

In order to analyse the influence of grain and grain boundary on the electrical properties of the crystalline LAGP samples (sintered at 560 °C and at higher temperatures), we fitted the impedance spectra to equivalent circuits using the Zview® (version 2.70) software. A representative equivalent circuit is shown in the inset of Fig. 8(A). The grain properties are represented by a parallel combination of a resistance R_g, a capacitance C_g and a constant-phase element CPE_g. The impedance of the constant-phase element (CPE) is given by: $Z_{CPE} = 1/Q(i\omega)^{-n}$ with $n \leq 1$. R_g and CPE_g are related to ionic motions in the grains: While R_g represents long-range ion transport, the constant-phase element CPE_g represents subdiffusive ion motions on microscopic length scales [42,43]. The capacitance C_g accounts for fast electronic and vibrational polarization in the grains. The grain boundary properties are described by a parallel combination of a resistance R_{gb} and a constant-phase element CPE_{gb}. The resulting grain boundary impedance acts in series to the grain impedance. Since our grain diameters (>30 nm) are much larger than the typ-

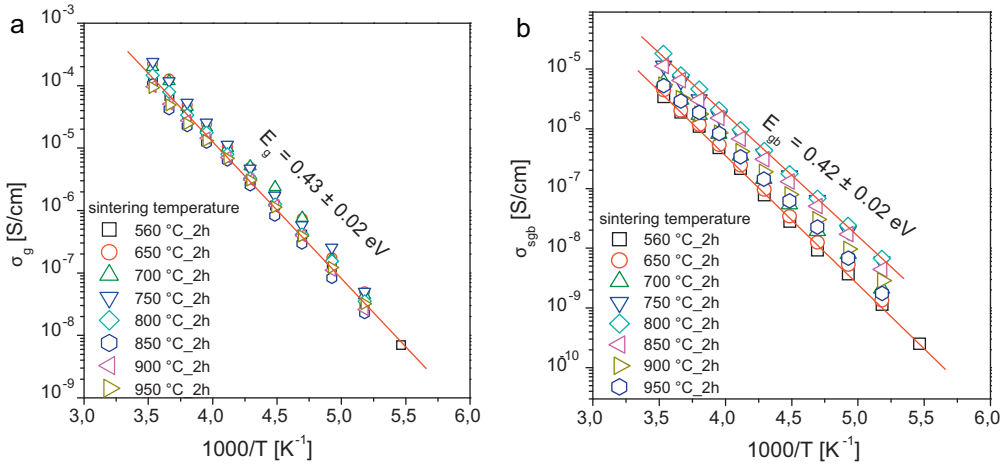

Fig. 10. (a) Arrhenius plots of the specific grain conductivity for samples sintered at temperatures between 560 °C and 950 °C for 2 h. (b) Arrhenius plot of the specific grain boundary conductivity of the samples, derived in the framework of the classical brick layer model.

ical thickness of a grain boundary, we assume that parallel grain boundary conduction is negligible. Finally, a constant-phase element CPE_{el} accounts for electrode polarization effects in the low frequency region.

In the framework of the classical brick layer model (BLM), the specific grain conductivity σ_g is calculated from the grain resistance R_g via:

$$\sigma_g = \frac{1}{R_g}\left(\frac{t}{A}\right) \quad (3)$$

As seen from Fig. 10(a), the grain conductivity and its activation energy is essentially independent of the sintering temperature. This reveals that although the cell volume of LAGP depends weakly on the sintering temperature (XRD analysis), the lithium ion transport in the grains is not significantly influenced by this effect.

In order to calculate the serial grain boundary conductivity, we assumed that the permittivity of grains and of grain boundaries is identical. In this case, the ratio of grain capacitance to grain boundary capacitance is given by: $C_g/C_{gb} = d/D$, where d is thickness of a grain boundary, and D is diameter of a grain. The grain boundary capacitance C_{gb} was derived from the equivalent circuit fit according to $C_{gb} = (R_{gb}{}^{1-n}Q_{gb})^{1/n}$ [22]. In the framework of the classical BLM, this results in the following equation for the specific grain boundary conductivity σ_{gb}:

$$\sigma_{gb} = \frac{1}{R_{gb}}\left(\frac{t}{A}\right)\left(\frac{d}{D}\right) \quad (4)$$

As seen from Fig. 10(a) and (b), σ_{gb} is influenced by the sintering temperature of the samples and is 1–2 orders of magnitude lower than the grain conductivity σ_g. Remarkably, the activation energies of σ_{gb} and σ_g are virtually identical, but their pre-exponential factor differs considerably. This suggests that ion blocking effects at the grain boundaries are not caused by high activation barriers, but by geometrical constriction effects.

In Fig. 11, we summarize the dependence of the grain conductivity σ_g, of the grain boundary conductivity σ_{gb}, and of the total conductivity σ_t on the sintering temperature. The plot reveals that the maximum of total conductivity found for the sample sintered at 750 °C is related to a maximum of the grain boundary conductivity σ_{gb}.

In Table 3, we give values for the grain size, for the capacitance ratio C_g/C_{gb} and for the thickness of the grain boundaries derived from the classical BLM equation: $C_g/C_{gb} = d/D$. Remarkably, the calculated grain boundary thickness increases with increasing sintering temperature. For the samples sintered at 850 °C and

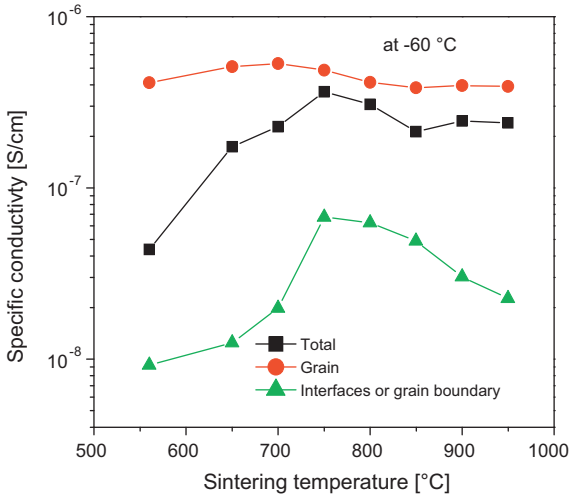

Fig. 11. Total conductivity, grain conductivity and grain boundary conductivity (derived from the classical BLM) versus sintering temperature.

900 °C, d is larger than 6 nm. In this model, it is assumed that the contact area between two grains is identical to the square of the grain diameter (grains are represented by cubes with perfect contact). However, our TEM pictures (Fig. 7) reveal that the real contact area between the grains is considerably smaller.

The influence of such imperfect grain contacts on the grain boundary resistance was analysed by Fleig et al. using the finite element method [21]. The following assumptions were made: (i) Only a fraction α of the surface area of a grain has perfect contact to neighboring grains. (ii) At the perfect contacts, the specific electrical properties (conductivity and permittivity) are identical to those of the grains. These assumptions imply that there is a purely geometrical current constriction effect at the perfect contacts, so that

Table 3
Sintering temperature, mean grain sizes, ratio of grain to grain boundary capacitance, thickness of the grain boundaries for the LAGP samples (calculated from the classical BLM).

Sintering temperature	Grain size, D (nm)	C_g/C_{gb}	d (nm)
560 °C	44	0.055	2.42
650 °C	55	0.059	3.25
750 °C	76	0.055	4.18
850 °C	98	0.069	6.76
950 °C	194	0.033	6.40

the activation energies of grain and grain boundary resistance are identical. This is in agreement with our experimental results. Fleig et al. derive the following approximate relation for the resistance ratio R_{gb}/R_g:

$$\frac{R_{gb}}{R_g} \approx \frac{1}{\sqrt{4\alpha_{contact} n}} \quad (5)$$

with n being the average number of contacts between two grains. The TEM pictures in Fig. 7 suggest that $n = 1$. In this case Eq. (5) can be simplified to

$$\frac{R_{gb}}{R_g} \approx \frac{1}{\sqrt{4\alpha_{contact}}} \quad (6)$$

Our impedance spectra (Fig. 8) show that the resistance ratio R_{gb}/R_g is close to unity, implying that $\alpha_{contact} < 0.25$. This appears to be also in good agreement with our TEM results. A major part of the surface adjoins to pores, to residual amorphous phase and to impurity phases (GeO_2, $AlPO_4$) and is thus insulating with respect to ion transport.

In the case of purely geometrical current constriction, the grain boundary capacitance is determined by the non-contact surface area of the grains. When in our samples, the relative amount of non-contact area is >0.75, the classical BLM relation $C_g/C_{gb} = d/D$ should hold in a good approximation. However, it is important to note that the thickness parameter d derived from this relation does not represent the grain boundary thickness at the contact areas, but the thickness of the insulating regions between the non-contact areas. These insulating regions can be pores, residual amorphous phases and impurity phases. A comparison with our TEM pictures (Fig. 7) reveals that d values in the range of several nm are reasonable. The increase of d with increasing temperature reflects most likely the increasing amount of pores and impurity phases in samples sintered at higher temperatures.

4. Conclusions

We have prepared $Li_{1.5}Al_{0.5}Ge_{1.5}(PO_4)_3$ (LAGP) ceramics with different grain sizes by means of the flash creation method and a subsequent sintering process. The cell volumes obtained from powder XRD depend weakly on the sintering temperature and increase from 1212.89 Å^3 at 520 °C to 1224.31 Å^3 at 850 °C. The relative density of the LAGP samples is about 83% in a sintering temperature range from 600 °C to 800 °C and decreases strongly above 800 °C due to formation of pores and of impurity phases (mainly GeO_2 and $AlPO_4$).

The lithium ion transport in samples sintered at 520 °C and 540 °C is impeded by residual amorphous phase. Samples sintered at 540 °C and higher temperatures are predominantly crystalline and exhibit a high total conductivity being typical for materials with NASICON structure. A maximum total conductivity of 2×10^{-4} S cm^{-1} at room temperature was found for a sample sintered at 750 °C.

In order to distinguish between the influence of grain and grain boundaries on the ion transport, AC impedance spectra were taken and fitted to equivalent circuits. The results were analysed in the framework of the classical brick layer model and a finite-element approach taking into account geometrical current constriction due to imperfect grain contacts. Such imperfect grain contacts are seen in TEM pictures of our samples. The predictions of the finite-element approach for the ratio of grain and grain boundary resistances are in good agreement with our experimental results. The grain boundary capacitance provides information about the thickness of insulating regions between the non-contact surface area of the grains. The thickness is in the range of a few nm and increases with increasing temperature. This temperature dependence is most likely caused by an increasing amount of pores and impurity phases with increasing sintering temperature.

Acknowledgments

We are grateful to Prof. Klaus Harms, University of Marburg, for the X-ray diffraction measurements; to Dr. Sima Haddadpour and Mr. Thomas Kaib for the TGA-DSC measurements and to Mr. M. Hellwig for the SEM measurements.

References

[1] J.-M. Tarascon, M. Armand, Nature 414 (2001) 359–367.
[2] P. Knauth, Solid State Ionics 180 (2009) 911–916.
[3] H. Aono, N. Imanaka, G.-Y. Adachi, Acc. Chem. Res. 27 (1994) 265–270.
[4] L. Sebastian, J. Gopalakrishnan, J. Mater. Chem. 13 (2003) 433–441.
[5] U.v. Alpen, A. Rabeneu, G.H. Talat, Appl. Phys. Lett. 30 (1977) 621–623.
[6] A.R. Rodger, J. Kuwano, A.R. West, Solid State Ionics 15 (1985) 185–198.
[7] B. Bates, N.J. Dudney, G.R. Gruzalski, R.A. Zuhr, A. Choudhury, C.F. Luck, Solid State Ionics 53–56 (1992) 647–654.
[8] S. Kondo, K. Takada, Y. Yamamoto, Solid State Ionics 53–56 (1992) 1183–1186.
[9] G.-Y. Adachi, N. Imanaka, H. Aono, Adv. Mater. 8 (1996) 127–135.
[10] S. Stramare, V. Thangadurai, W. Weppner, Chem. Mater. 15 (2003) 3974–3990.
[11] V. Thangadurai, A.K. Shukla, J. Gopalakrishnan, J. Mater. Chem. 9 (1999) 739–741.
[12] M. Sugantha, U.V. Varadaraju, Solid State Ionics 95 (1997) 201–205.
[13] C.J. Leo, G.V. Subbarao, B.V.R. Chowdari, J. Mater. Chem. 12 (2002) 1848–1853.
[14] J.B. Goodenough, H.Y.-P. Hong, A. Kafalas, Mater. Res. Bull. 11 (1976) 203–220.
[15] C.R. Mariappan, G. Govindaraj, B. Roling, Solid State Ionics 176 (2005) 723–729.
[16] N. Machida, K. Fujii, T. Minami, Chem. Lett. (1991) 367–370.
[17] H. Aono, E. Sugimoto, Y. Sadaoka, Bull. Chem. Soc. Jpn. 65 (1992) 2200–2204.
[18] J.E. Bauerle, J. Phys. Chem. Solids 30 (1969) 2657–2670.
[19] R. Bouchet, P. Knauth, J.-M. Laugier, J. Electrochem. Soc. 150 (2003) E348–E354 (J. Electroceram. 16 (2006) 229–238).
[20] N.J. Kidner, N.H. Perry, T.O. Mason, J. Am. Ceram. Soc. 91 (2008) 1733–1746.
[21] J. Fleig, J. Maier, J. Am. Ceram. Soc. 82 (1999) 3485–3494.
[22] J. Fleig, Solid State Ionics 131 (2000) 117–127.
[23] J. Fu, Solid State Ionics 104 (1997) 191–194.
[24] J.S. Thokchom, B. Kumar, J. Power Sources 195 (2010) 2870–2876.
[25] B.V.R. Chowdari, G.V. Subbarao, C.J. Leo, Solid State Ionics 136–137 (2000) 1067–1075.
[26] A.M. Cruz, E.B. Ferreira, A.C.M. Rodrigues, J. Non-Cryst. Solids 355 (2009) 2295–2301.
[27] S.-C. Li, J.-Y. Cai, Z.-X. Lin, Solid State Ionics 28–30 (1988) 1265–1270.
[28] M. Cretin, P. Fabry, J. Eur. Ceram. Soc. 19 (1999) 2931–2940.
[29] P.M. Manso, M.C.M. Sedeno, S. Bruque, J. Sanz, E.R. Lossilla, Solid State Ionics 178 (2007) 43–52.
[30] X. Xu, Z. Wen, X. Wu, X. Yang, Z. Gu, J. Am. Ceram. Soc. 90 (2007) 2802–2806.
[31] M. Kakihana, M. Yoshimura, Bull. Chem. Soc. Jpn. 72 (1999) 1427–1436.
[32] A. Watanabe, T. Fukui, K. Nogi, Y. Kizaki, Y. Noguchi, M. Miyayama, J. Ceram. Soc. Jpn. 114 (2006) 97–101.
[33] http://www.hosokawamicron.co.jp/en/powder/p-design/p-design/nanocreater/.
[34] J. Rodriguez-Carvajal, Physica B 192 (1993) 55–69.
[35] G.K. Williamson, W.H. Hall, Acta Metall. 1 (1953) 22–31.
[36] M. Catti, A. Comotti, S.D. Blas, R.M. Ibberson, J. Mater. Chem. 14 (2004) 835–839.
[37] J. Haines, J.M. Léger, C. Chateau, A.S. Pereira, Phys. Chem. Miner. 27 (2000) 575–582.
[38] R.C.E. Mooney, Acta Cryst. 9 (1956) 728–734.
[39] I.-W. Chen, X.H. Wang, Nature 404 (2000) 168–171.
[40] D.M. Roy, G.R. Gouda, J. Am. Ceram. Soc. 56 (1973) 549–550.
[41] J.S. Thokchom, B. Kumar, J. Power Sources 185 (2008) 480–485.
[42] K. Funke, C. Cramer, B. Roling, T. Saatkamp, D. Wilmer, M.D. Ingram, Solid State Ionics 85 (1996) 293–303.
[43] J.C. Dyre, P. Maass, B. Roling, D.L. Sidebottom, Rep. Prog. Phys. 72 (2009) 046501.